Heliyon 10 (2024) e35885

Contents lists available at ScienceDirect

Heliyon

journal homepage: www.cell.com/heliyon

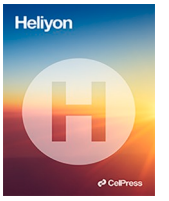

Research article

Performance studies of an ultrafast gamma Cherenkov imaging Screen based on Silica fibers array

Zhang Mei [a,*], Yang Li [a], Yan Song [a], Liang Sheng [a], Quan Guo [a], Yi Hong Yan [b], Hong Qiao Yin [a]

[a] State Key Lab of Intense Pulsed Radiation Simulation and Effect, Northwest Institute of Nuclear Technology, Shanxi, Xi'an, 710024, China
[b] School of Energy and Power Engineering, Xi'an Jiaotong University, Xi'an, 710049, China

ARTICLE INFO

Keywords:
Cherenkov radiation
Ultrafast gamma imaging
Silica fibers array
Radiation detector

ABSTRACT

High-energy gamma rays produced in inertial confinement fusion (ICF) experiments are crucial for studying implosion dynamics. These gamma rays, characterized by their extremely short durations, represent the least disturbed products of fusion, preserving vital birth information. To detect such γ-rays, ultrafast radiation detectors with high time resolution are necessary. This study introduces a newly developed Cherenkov optical image screen designed for ultra-fast gamma-ray imaging. Composed of pure quartz fiber material, the imaging screen features a single fiber pixel size of 0.6 mm and a thickness of 3 cm. Theoretical investigations explore the luminous time response and efficiency of the Cherenkov optical imaging screen under gamma-ray irradiation. Experimental validation was conducted using a steady-state gamma-ray source with an average energy of 1.25 MeV. Results demonstrate that the image screen achieves a spatial resolution limit of 0.75 mm. The temporal response exhibits a full width at half maximum of less than 0.4 ns when excited by a high-energy electron beam with a single pulse duration of several picoseconds.

1. Introduction

Several ultra-fast transient high-energy radiation facilities have been developed for diverse research objectives, such as the Institute of Laser Engineering at Osaka University [1], OMEGA-EP at the Laboratory for Laser Energetics at the University of Rochester [2], and Lawrence Livermore National Laboratory [3]. These facilities focus on Fast Ignition and Inertial Confinement Fusion (ICF) to achieve nuclear fusion energy from thermonuclear fuels, primarily deuterium and tritium, under conditions of high temperature and pressure. In ICF, encapsulated fusion fuel undergoes compression and heating to extreme densities, temperatures, and pressures, facilitating rapid fusion reactions before disassembly [3,4]. The yield of these reactions depends significantly on compression size and spherical symmetry, necessitating diagnostic tools with spatial sensitivity [5,6]. Gamma imaging systems are utilized to gather data on radiation spot size and shape, which is crucial for diagnosing implosion symmetry. For instance, the $^{12}C(n,n'\gamma)^{12}C$ reactions in residual debris from polymer ablators emit substantial fluence of 4.44 MeV gamma rays. Images of these gamma rays from the $^{12}C(n, n'\gamma)^{12}C$ reactions in plastic ablator shells aid in assessing the symmetry of the ablation process [4,5].

For ICF, gamma rays are emitted with very short durations (~1 ns) [7–9]. Ultra-fast gamma imaging serves as a critical diagnostic

* Corresponding author.
E-mail addresses: zandwnever@163.com, zhangmei@nint.ac.cn (Z. Mei).

https://doi.org/10.1016/j.heliyon.2024.e35885
Received 19 February 2024; Received in revised form 26 July 2024; Accepted 6 August 2024
Available online 8 August 2024

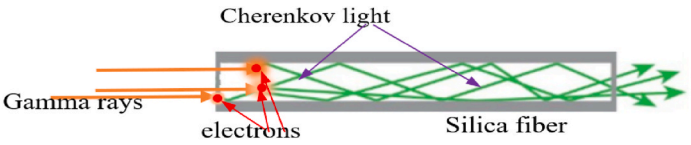

(a) Schematic of Cherenkov radiation produced by gamma rays in an optical fiber

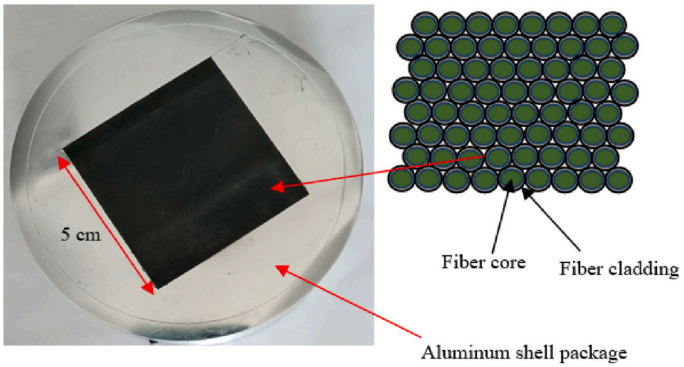

(b) Photograph of the silica optical fiber array screen(left) and the schematic of array (right)

Fig. 1. Schematic of Cherenkov radiation in optical fiber and the photograph of the silica optical fiber array screen.

tool capable of independently capturing time-resolved images, thereby revealing the temporal evolution of the 2D spatial structure of the radiation spot. Currently, commonly used inorganic and organic scintillators, which convert nuclear radiation into visible light, typically exhibit a slow decay component (ranging from tens of nanoseconds to microseconds). This limitation precludes their application in gamma imaging, requiring sub-nanosecond time resolution scales [10–12]. Improved time performance can be achieved by focusing on promptly emitted photons, such as Cherenkov Radiation (CR). CR is electromagnetic shockwaves generated when charged particles move faster than the speed of light in a medium [13]. Pavel A. Cherenkov, Il'ja M. Frank, and Igor Y. Tamm received the Nobel Prize in Physics in 1958 for their discovery and explanation of Cherenkov radiation [14–16]. Since then, CR has found applications in various fields, including particle detection [17], terahertz sources [18], medical imaging [19], and phototherapy [20]. Recent studies have explored CR phenomena extensively, utilizing free electrons interacting with nanostructures or novel mechanisms to achieve efficient CR generation, even from low-energy electrons [21–24]. Over the past decade, Cherenkov detectors for ultrafast nuclear radiation have been crucial in ICF research, offering time responses on the order of 0.1 ns. Examples include Gas Cherenkov Detectors (GCD) or Gamma Reaction History (GRH) detectors used to measure the history of deuterium–tritium reactions [D(t, γ)^{5}He] from 16.75 MeV gamma rays [25–27]. This reaction history provides critical data such as bang time and burn width to assess implosion performance and validate ICF simulations. Silica fiber is particularly suitable for Cherenkov light production, especially in hazardous, radioactive environments, due to its low radiation-induced loss. Many studies focus on pure silica core fibers as Cherenkov detectors [28,29]. Previous research has shown that gamma ray-induced luminescence in pure silica fibers is primarily due to Cherenkov radiation, generated by secondary electrons resulting from interactions between gamma rays and silicon materials (specifically, the photoelectric effect, Compton effect, and electron pair production; Compton effect predominates for gamma rays with energies between 1 MeV and 10 MeV) [30]. Therefore, this paper explores the performance of an array image screen composed of optical fiber array materials.

2. Cherenkov radiation in silica fiber array screen

Cherenkov radiation arises from the transient polarization of a medium as a charged particle moves faster than the speed of light within that medium. The Cherenkov radiation is produced in materials if the energy of the particle is higher than a certain threshold that is given by $(1/\beta n)$, where n is the refractive index of the medium and β is the ratio between the particle velocity and the speed of light in vacuum [14–16]. Frank and Tamm showed that the energy W radiated by the electron through the surface of a cylinder of length l is [31]

$$W = \frac{e^2 l}{c^2} \int_{n\beta>1} \omega \mathrm{d}\omega \left(1 - \frac{1}{n^2\beta^2}\right) \tag{1}$$

The angular frequency of Cherenkov radiation, denoted as ω, is given by $\omega = 2\pi c/\lambda$, where λ is the wavelength of the emitted

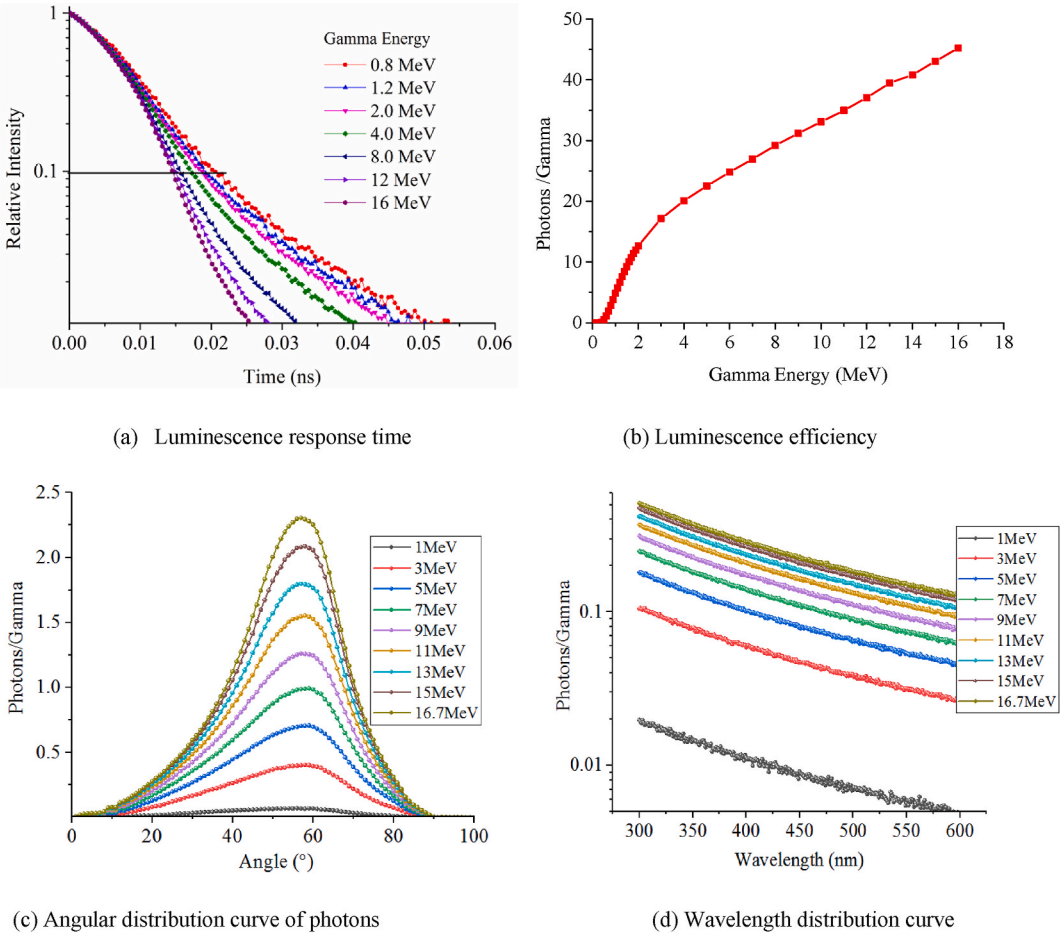

(a) Luminescence response time

(b) Luminescence efficiency

(c) Angular distribution curve of photons

(d) Wavelength distribution curve

Fig. 2. Luminescence response time, luminescence efficiency, angular distribution curve, and wavelength distribution of photons emitted at the fiber output end by simulation.

Cherenkov radiation and *c is* the speed of light. According to the principle of Cherenkov radiation, in certain high-energy physics and astrophysics experiments, high-energy particles or radiation can emit Cherenkov light, which appears as visible light signals that can be easily recorded. Fig. 1(a) depicts a diagram of Cherenkov light emission in a fiber under gamma-ray irradiation.

The fiber array consists of pure silica core fibers with a diameter of 600 μm and F-doped silica cladding, arranged in a hexagonal (honeycomb) pattern to form a square array that is 3.0 cm thick (manufactured by Chunhui Technology Co., Ltd., China). Taking into account efficiency and spatial resolution considerations, the array thickness is set at 3 cm. Each fiber has a cladding thickness of 0.06 mm. The core refractive index is 1.458, and the numerical aperture (NA) is 0.22. The cladding refractive index is 1.441. The active imaging area of the array measures 5 cm × 5 cm. In Fig. 1(b), the left panel displays a photograph of the fiber array screen, while the right panel illustrates a schematic of the fiber array. The peripheral parts of the fiber array screen are enclosed in an aluminum shell. According to Cherenkov radiation theory, for Cherenkov light produced in silica material (with a refractive index of 1.458), the incident electrons need to have an energy greater than 0.2 MeV, and incident gamma rays need to have an energy greater than 0.3 MeV (based on the Compton scattering formula, which produces electrons with an average energy of 0.2 MeV from incident gamma rays with about 0.3 MeV energy).

When gamma rays penetrate the fiber array, they interact with the fibers, generating high-energy electrons. As these electrons move through the fiber material, they emit visible light signals through the Cherenkov radiation process. This conversion of gamma rays into visible light occurs within the fiber array, facilitating spatial radiation distribution and imaging.

The Monte Carlo simulation program using Geant4 software simulated the luminescence response time and efficiency of the array screen under gamma-ray irradiation. In the simulation setup, a surface source of gamma rays collimated to 2 mm diameter was configured to irradiate perpendicularly onto the input face of the fiber array. The program recorded the time and energy of each Cherenkov photon on the output surface of the fiber array, accounting for the spectral response characteristics of the actual detector used. Specifically, only Cherenkov photons with wavelengths between 300 nm and 600 nm were recorded based on their photon type and energy. The simulation also incorporated the attenuation of Cherenkov photons in quartz optical fibers, considering the material's wavelength-dependent photon attenuation characteristics and transmission distances. Various gamma ray-matter interactions, such as

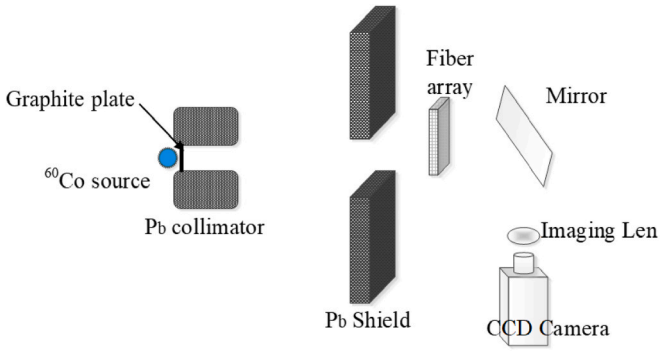

Fig. 3. Schematic diagram of the experimental setup for fiber array at ^{60}Co source (The scintillator (not shown) is placed in the same position).

the electron pair effect, Compton effect, and photoelectric effect, were included in the simulation. The dominant interaction was the Compton effect, which primarily produced the electrons responsible for generating Cherenkov light. Within the Geant4 software, the simulation detailed the transport and interaction processes of electrons, as well as the propagation of Cherenkov light within the quartz fiber material, utilizing relevant physical models and simulation packages.

Fig. 2(a) illustrates the temporal distribution of luminescent photons under gamma-ray irradiation at different energies, depicting luminescence response time curves. These curves show how Cherenkov photons from the output end of the optical fiber array vary over time, normalized to their maximum values. Notably, the time corresponding to one-tenth of the peak intensity on the trailing edge of these curves (indicated by the intersection of a black horizontal line with the curves on the time axis) is less than 0.03 ns, decreasing with increasing gamma-ray energy. Higher-energy gamma rays generate secondary electrons with greater energy, enabling faster transmission through the optical fiber arrays. Consequently, the photons produced exhibit less temporal dispersion over time.

Fig. 2(b) displays the number of Cherenkov photons produced versus the energy of gamma rays, normalized per gamma photon. This characterization represents the efficiency of luminescence with respect to gamma photons of varying energies, showing an increase with higher gamma-ray energies. According to the simulation results, the efficiency is notably low for lower energy gamma rays: only 10^{-4} photons per gamma photon are produced for 0.2 MeV gamma rays, and this increases to 10^{-2} photons per gamma photon for 0.3 MeV gamma rays. As the energy of gamma rays reaches 0.6 MeV, one photon per gamma photon can be obtained, and about 4 photons per gamma photon are produced at 1 MeV gamma-ray energy.

Fig. 2(c) illustrates the angular distribution curve of photons emitted at the output end of the optical fiber under gamma-ray irradiation of various energies, normalized per gamma photon. The emission direction of the photons is perpendicular to the end face of the optical fiber, with the emission angle defined as 0°. In the simulated fiber model, there is no light-absorbing coating outside the fiber cladding. The photons that meet the conditions for light transmission within the optical fiber, including Cherenkov light generated from the fiber cladding and photons refracted from the core through the cladding, are counted. The distribution shows that the majority of Cherenkov radiation photons emitted from the fiber are concentrated between 40° and 60° emission angle.

Fig. 2(d) depicts the wavelength distribution of output Cherenkov light versus the energy of gamma rays, normalized per gamma photon. The graph illustrates that the number of Cherenkov photons generated decreases as the wavelength increases, correlating with the law of Cherenkov radiation intensity as a function of wavelength. This trend is consistent with the characteristic behavior where shorter wavelengths correspond to higher photon emission frequencies and vice versa.

3. Results and discussion

3.1. Experiment setup for radiation imaging

The performance evaluation of the optical fiber array was conducted using a^{60}Co source, which releases electrons through beta decay with energies up to 0.315 MeV and emits gamma rays at energies of 1.17 MeV and 1.33 MeV. The source activity is 4000 Ci. To attenuate electrons significantly, a 5 mm thick graphite plate was inserted into the collimation channel, ensuring that the rays passing through the collimator (seen in Fig. 3, labeled as Pb collimator) are predominantly gamma photons. Fig. 3 illustrates the experimental setup, where a mirror directs Cherenkov light from the optical fiber array into a camera imaging system comprising a Canon EF 50 mm f/1.2 lens coupled to a cooled Andor camera equipped with an intensifier. The distances from the gamma source to the fiber array, fiber array to mirror, and mirror to the camera are 3.5 m, 0.2 m, and about 0.5 m, respectively. The camera system, essential throughout the measurement series, was housed in a lead-shielded room constructed with 20 cm thick lead bricks. On the output surface of the fiber array, the spatial resolution sampled by the camera imaging system is 0.07 mm per pixel. For comparison of light intensity or relative sensitivity, a conventional plastic scintillator BC408 (10 mm thick, manufactured by Saint-Gobain, France) with a fast decay time of 2.4 ns was employed.

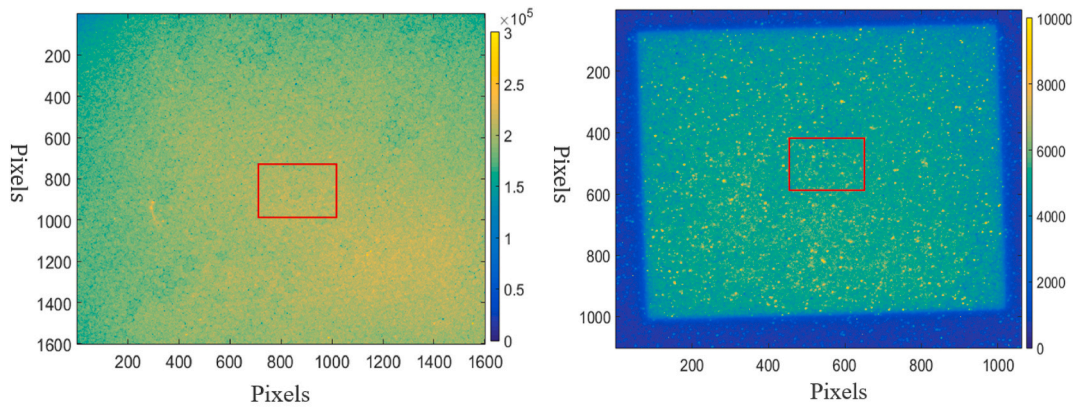

(a) 1 cm thick BC408 scintillator (b) 3 cm thick fiber array.

Fig. 4. Illumination image of both image screens under the ^{60}Co source irradiation (The red rectangle box shows the area of the image selected for sensitivity comparison).

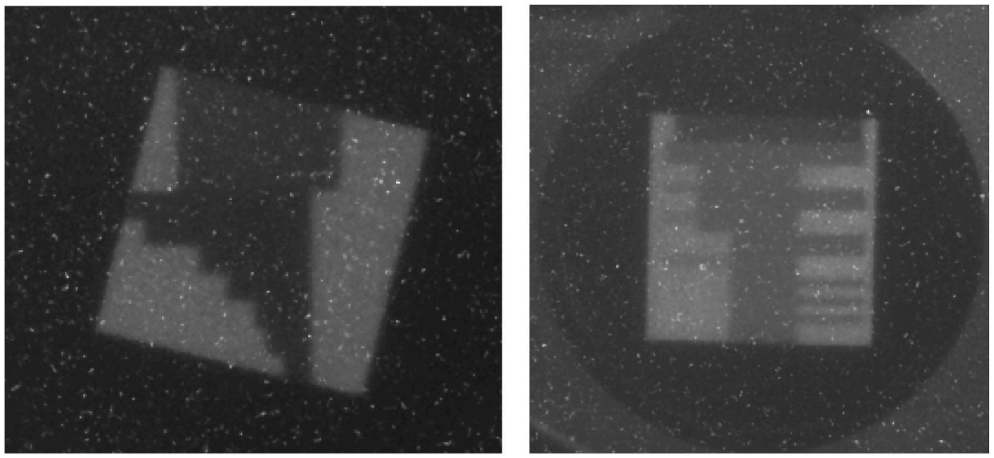

(a) 5 mm tungsten step block (b) 2 mm thick tungsten resolution card

Fig. 5. Radiographic image of two test objects.

3.2. Relative gamma sensitivity

Fig. 4 presents radiographic images of both the BC408 scintillator (Fig. 4(a)) and the optical fiber array (Fig. 4(b)) directly irradiated by gamma rays. In Fig. 4(b), the blue-colored region with low gray levels around the image periphery is attributed to background scattering from gamma irradiation in the aluminum shell (as depicted in Fig. 1). The exposure time for both radiographs was identical, set at 10,000 s. To estimate relative output light intensity, the average gray value of pixels within the red rectangular region in both Fig. 4 images was calculated. The gamma beam intensity varied by no more than 2 % across imaging frames, ensuring direct evaluation of the raw radiographs for sensitivity comparison.

Comparing the average grayscale values within the red boxes of the two radiographic images, we find they are 19,600 for Fig. 4(a) (BC408 scintillator) and 4900 for Fig. 4(b) after subtracting background noise (optical fiber array). This comparison suggests that the sensitivity of the 10 mm thick BC408 scintillator is roughly 40 times higher than that of the optical fiber array.

3.3. Radiographic imaging and evaluation of the spatial resolution

To validate the feasibility of radiation imaging using the fiber array, test objects, including a 10 mm thick tungsten step block and a 5 mm thick tungsten resolution card, were utilized in the experimental setup depicted in Fig. 3. These objects were positioned near the front face of the fiber array screen, directly exposed to radiation. Fig. 5 presents radiographic images captured with the optical fiber

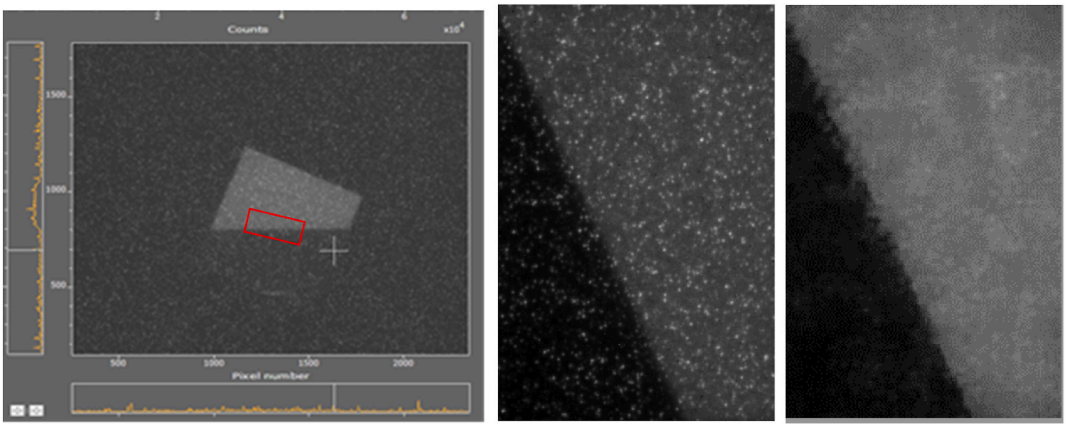

(a) Knife-edge original ESF image (b) Clipped image from the red box (c) Denoised ESF image

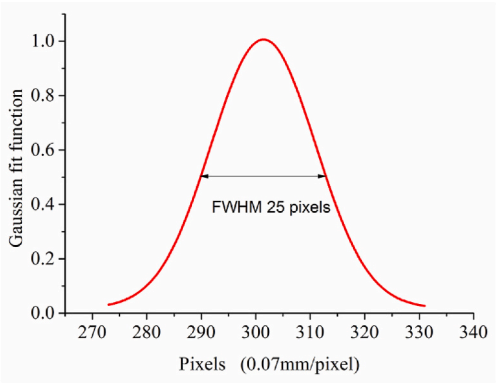

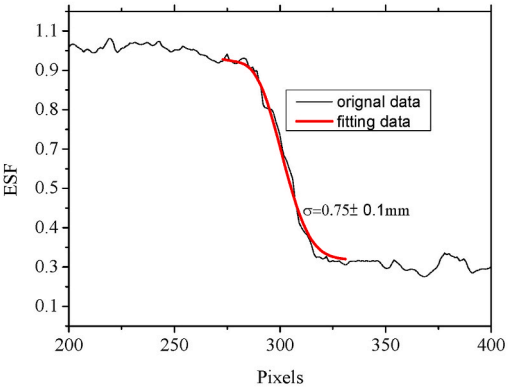

(d) Gaussian fitting curve of LSF curve (e) Original ESF curve and fitting curve

Fig. 6. Radiographic image of the tungsten block and ESF.

array. Fig. 5(a) shows the radiographic image of the 5 mm tungsten step block, while Fig. 5(b) displays the image of the 2 mm thick tungsten resolution card. Both images accurately depict the projected images of gamma rays passing through the test objects, demonstrating the capability of the array screen for radiographic imaging based on the Cherenkov luminescence effect. It is noted that due to the scattering of high-energy gamma rays, background noise arising from the direct interaction between scattered gamma rays and the camera is present in the images.

The spatial resolution capability of an image detector is often assessed using a point spread function (PSF). However, accurately determining the exact shape of the PSF can be challenging. Typically, this is achieved through a method known as the knife-edge input method. This method relies on the principle that a knife-edge will stimulate the imaging system across all spatial frequencies. The resulting profile of the edge is called the edge spread function (ESF), which represents the projection of the 2D PSF along the edge's normal direction. By differentiating the ESF, a line spread function (LSF) can be derived. The LSF, which is typically Gaussian in shape, can be characterized by a single parameter—its standard deviation σ:

$$LSF(x) = \frac{1}{\sqrt{2\pi}\sigma} e^{-x^2/2\sigma^2} \tag{2}$$

The standard deviation of the measured LSF (σ) is used to characterize the spatial resolution of the image detector.

We employed a 5 cm thick tungsten block with a straight edge to capture the ESF image for measuring imaging resolution. The thickness of the tungsten block ensures effective attenuation of gamma-ray transmission. As a result, the radiograph displays a dark region where gamma rays were blocked by the tungsten object, contrasting with a light region where gamma rays interacted with the fiber array without obstruction.

In the described experimental setup, a 5 cm thick tungsten block was positioned near the front of the optical fiber array, with its edge oriented at an angle relative to the array's direction. Fig. 6(a) shows the resulting radiographic image of gamma rays passing through the tungsten block, referred to as the knife-edge or ESF image. Fig. 6(b) displays an ESF image cropped from the red rectangular area in Fig. 6(a), rotated and stretched by a factor of 7. Due to the fiber array's low light yield, a high camera gain was

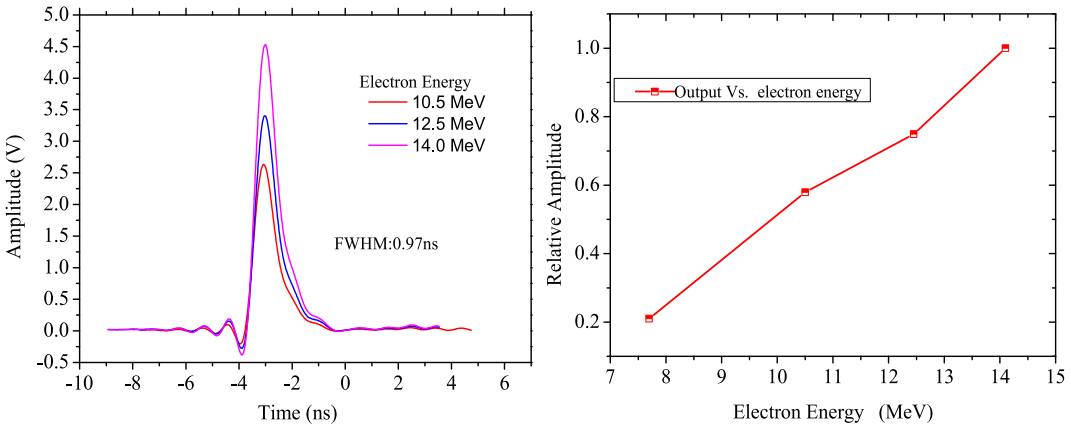

(a) Electronic impulse response waveform (b) Relative amplitude Versus electron energy

Fig. 7. Time response waveforms and relative amplitude under ultrashort electron beams irradiation with various energy.

necessary, resulting in noticeable noise levels in the captured image (Fig. 6(b)). To reduce this noise, a Non-Local Means filter method was applied, resulting in the denoised ESF image shown in Fig. 6(c) [32]. To obtain a smoother ESF curve, the denoised ESF underwent differentiation to derive a LSF curve. Using equation (2), the LSF curve was fitted with a Gaussian function, and integration of this function yielded the fitted ESF curve. Fig. 6(e) presents both the original ESF curve and the fitted ESF (red line), demonstrating good agreement between the two curves in the primary section. According to Ref. [33], the spatial resolution for the system is defined as the Gaussian standard deviation σ. Thus, in the light of the Gaussian curve in Fig. 6(d), $\sigma \approx 10.6$ pixels, and 0.07 mm/pixel, the limit spatial resolution for the fiber array is estimated at about 0.75 mm.

3.4. Evaluation of luminescence time response

The quartz fiber array's emission time response was evaluated using a high-intensity pulsed electron linac. This linac emits electron pulses at 10 Hz, each carrying a charge of about 0.5–1.0 nC and lasting less than 10 ps. The beam energy can be adjusted from 4 MeV to 120 MeV with an energy spread of less than 0.3 %. Due to their extremely narrow time widths compared to the detection system's response functions, each electron pulse can be treated as a Dirac function pulse. In the experimental setup, the emission characteristics of the fiber array were examined using a photoelectric tube (PT:H9305–03, Hamamatsu Photonics) and single pulse electron beam excitation. The photoelectric tube converts Cherenkov light signals from the fiber array into electrical signals, which were then captured by an oscilloscope (sampling rate of 5 G/s, bandwidth of 1 GHz). The photoelectric tube's spectral sensitivity spans from 185 nm to 900 nm, peaking around 450 nm, with a time response characterized by a full width at half maximum (FWHM) of 0.8 ns. Furthermore, an integrating current transformer (ICT) was utilized to monitor the charge per electron beam pulse.

Under the influence of a single pulsed electron beam, the time response characteristics of the fiber array were evaluated by analyzing the output waveform detected by the photoelectric tube. Fig. 7(a) depicts the recorded signal waveform of Cherenkov light emitted by the fiber array when irradiated with single electron pulses of varying energies. The FWHM of this waveform measures 0.97 ns. This value accounts for contributions from the duration of the electron pulse, the inherent time response of the fiber array screen, the characteristics of the detector and transmission line, as well as the bandwidth limitations of the oscilloscope and signal connectors. To estimate the FWHM of the fiber array's response time, the square of the FWHM of the output waveform was considered as the sum of the squares of the FWHM of each component within the measurement setup. Subtracting the response times of the photoelectric tube detector (0.8 ns FWHM), the oscilloscope, and the transmission line (totaling about 0.45 ns FWHM) from the output waveform, an approximate FWHM of 0.31 ns for the fiber array's response time was deduced, which is less than 0.4 ns. Fig. 7(b) illustrates a plot depicting the light output as a function of incident electron energy, showing an increase with higher electron energies. For example, the Cherenkov light output from 11 MeV to 14 MeV electrons is respectively 3 and 5 times higher than that produced by 7.6 MeV electrons.

4. Conclusion

To meet the demands of diagnosing ultra-fast radiation sources, a new Cherenkov image screen has been developed using a pure quartz fiber array. Results from tests with steady-state gamma-ray sources and ultra-fast high-energy electron beams demonstrate the following: The image screen achieves a spatial resolution limit of 0.75 mm, and its light-emitting time response has a FWHM of less than 0.4 ns. In comparison to traditional scintillator conversion imaging screens, this screen capitalizes on the Cherenkov radiation effect, offering instantaneous response without prolonged luminescence decay. However, its luminous efficiency is nearly two orders of magnitude lower than that of general scintillators. Efforts to enhance gamma detection efficiency are focused on two main

approaches. Firstly, the research aims to improve the efficiency of generating secondary electrons by gamma rays within the fiber array. This involves studying materials that convert gamma rays to electrons, with the goal of enhancing electron conversion efficiency in the fiber array to boost luminous efficiency, though expected improvements are limited. Secondly, feasibility studies will explore novel mechanisms reported earlier [17–20] for developing new imaging detectors.

Data availability

All relevant data are available from the authors upon reasonable request.

CRediT authorship contribution statement

Zhang Mei: Writing – review & editing, Writing – original draft, Investigation, Formal analysis, Data curation, Conceptualization. **Yang Li:** Data curation. **Yan Song:** Investigation. **Liang Sheng:** Conceptualization. **Quan Guo:** Formal analysis. **Yi Hong Yan:** Formal analysis. **Hong Qiao Yin:** Resources.

Declaration of competing interest

The authors declare that they have no known competing financial interests or personal relationships that could have appeared to influence the work reported in this paper.

Acknowledgement

This work is supported by the National Natural Science Foundation of China (No. 11275155, No. 12175183).

References

[1] K. Mima, A. Yogo, S.R. Mirfayzi, Z. Lan, Y. Arikawa, Y. Abe, H. Nishimura, Laser-driven neutron source and nuclear resonance absorption imaging at ILE, Osaka University: review, Appl. Opt. 61 (9) (2022) 2398–2405, https://doi.org/10.1364/AO.444628.
[2] R. Betti, O. Hurricane, Inertial-confinement fusion with lasers, Nat. Phys. 12 (2016) 435–448, https://doi.org/10.1038/nphys3736.
[3] G.P. Grim, N. Guler, F.E. Merrill, G.L. Morgan, C.R. Danly, et al., Nuclear imaging of the fuel assembly in ignition experiments, Phys. Plasmas 20 (2013) 056320, https://doi.org/10.1063/1.4807291.
[4] C. Baudet Lemieux, G.P. Grim, H.B. Barber, B.W. Miller, D. Fasje, L.R. Furenlid, Investigation of the possibility of gamma-ray diagnostic imaging of target compression at NIF, Proc. SPIE8144, Penetrating Radiation Systems and Applications XII (2011) 814407, https://doi.org/10.1117/12.895765.
[5] D.A. Lemieux, H.B. Barber, G.P. Grim, T. Archuleta, V. Fatherley, D. Fastje, Testing of a gamma ray imaging system at the high intensity gamma source. Proc. SPIE 9211, Target Diagnostics Physics and Engineering for Inertial Confinement Fusion III (2014) 921105, https://doi.org/10.1117/12.2066254.
[6] Y. Kim, J.M. Mack, H.W. Herrmann, C.S. Young, G.M. Hale, et al., D-T gamma-to-neutron branching ratio determined from inertial confinement fusion plasmas, Phys. Plasmas 19 (2012) 056313, https://doi.org/10.1063/1.4718291.
[7] J.E. McMillan, A. Cole, A. Kirby, M.L. Ahnen, Scintillators and Cherenkov detectors for the registration of 10.8 MeV gamma rays, J. Phys. Conf. 763 (2016) 012011, https://doi.org/10.1088/1742-6596/763/1/012011.
[8] J.P. Hayward, C.L. Hobbs, Z.W. Bell, L.A. Boatner, R.E. Johnson, J.O. Ramey, G.E. Jellison, C.R. Lillard, Characterizing the radiation response of Cherenkov glass detectors with isotopic sources, J. Radioanal. Nucl. Chem. 295 (2013) 1143–1151, https://doi.org/10.1007/s10967-012-1898-4.
[9] Y. Kim, H.W. Herrmann, A.M. McEvoy, C.S. Young, C. Hamilton, D.D. Schwellenbach, R.M. Malone, M.I. Kaufman, A.S. Smith, Aerogel Cherenkov detector for characterizing the intense flash x-ray source, Cygnus, spectrum, Rev. Sci. Instrum. 87 (2016) 11E723, https://doi.org/10.1063/1.4960541.
[10] S.J. Min, Y.S. Kim, K.H. Ko, B.k. Seo, J.H. Cheong, C.H. Roh, S.B. Hong, Optimization of plastic scintillator for detection of gamma-rays: simulation and experimental study, Chemosensors 9 (239) (2021) 1–14, https://doi.org/10.3390/chemosensors9090239.
[11] L.P. He, L. Zhang, X. Luo, Y. Fang, Z.J. Wei, G.J. Chang, R.Z. Yang, S.Y. Liu, M. Su, D.X. Liu, B.X. Yu, X.P. Yang, X. Li, An optimal solvent of liquid scintillator for fast-neutron imaging applications, J. Lumin. (2014) 148256–148261, https://doi.org/10.1016/j.jlumin.2013.12.014.
[12] V.G. Kleinrath, M.S. Freeman, C.R. Hurlbut, F. Merrill, J.R. Tinsley, P. Volegov, C. Wilde, A liquid VI scintillator cell for fast-gated neutron imaging, Rev. Sci. Instrum. 89 (2018) 101142, https://doi.org/10.1063/1.5039362.
[13] P.A. Cherenkov, Visible Emission of Clean Liquids by Action of γ Radiation, vol. 2, Dokl. Akad. Nauk. SSSR, 1934, p. 252.
[14] P.A. Cherenkov, Radiation of particles moving at a velocity exceeding that of light, and some of the possibilities for their use in experimental, in: Nobel Lectures, Physics 1942-1962, World Scientific Publishing, Singapore, 1998, pp. 426–441, https://doi.org/10.1142/3728, 1998.
[15] I.M. Frank, Optics of light sources moving in refractive media, in: Nobel Lectures, Physics 1942-1962, World Scientific Publishing, Singapore, 1998, pp. 442–469, https://doi.org/10.1142/3728, 1998.
[16] I.Y. Tamm, General characteristics of radiations emitted by systems moving with super-light velocities with some applications to plasma physics, in: Nobel Lectures, Physics 1942-1962, World Scientific Publishing, Singapore, 1998, pp. 470–483, https://doi.org/10.1142/3728, 1998.
[17] J.P. Hayward, Z.W. Bell, L.A. Boatner, C.L. Hobbs, R.E. Johnson, J.O. Ramey, G.E. Jellison, Simulated response of Cherenkov glass detectors to MeV photons, J. Radioanal. Nucl. Chem. 295 (2013) 1321–1329, https://doi.org/10.1007/s10967-012-1909-5.
[18] J. Zhang, X.F. Hu, H.S. Chen, F. Gao, Designer Surface Plasmons Enable Terahertz Cherenkov Radiation (Invited), PIER, vol. 169, 2020, pp. 25–32, https://doi.org/10.2528/PIER20102708.
[19] T.M. Shaffer, E.C. Pratt, J. Grimm, Utilizing the power of Cerenkov light with nanotechnology, Nat. Nanotechnol. 12 (2017) 106–117.
[20] N. Kotagiri, G.P. Sudlow, W.J. Akers, S. Achilefu, Breaking the depth dependency of phototherapy with Cerenkov radiation and low-radiance-responsive nanophotosensitizers, Nat. Nanotechnol. 10 (2015) 370–379.
[21] Z. Gong, J.L. Chen, R.X. Chen, X.J. Zhu, C. Wang, X. Y Zhang, H. Hu, Y. Yang, B.L. Zhang, H.S. Chen, I. Kaminer, X. Lin, Interfacial Cherenkov radiation from ultralow-energy electrons, Proc. Natl. Acad. Sci. U.S.A. 120 (38) (2023) e2306601120, https://doi.org/10.1073/pnas.2306601120.
[22] X. Lin, S. Easo, Y.C. Shen, H.S. Chen, B.L. Zhang, J. Joannopoulos, M. Soljačić, I. Kaminer, Controlling Cherenkov angles with resonance transition radiation, Nat. Phys. 14 (2018) 816–821, https://doi.org/10.1038/s41567-018-0138-4.
[23] X. Lin, H. Hu, S. Easo, Y. Yang, Y.C. Shen, K.Z. Yin, M.P. Blago, I. Kaminer, B.L. Zhang, H.S. Chen, J. Joannopoulos, M. Soljačić, Y. Luo, A Brewster route to Cherenkov detectors, Nat. Commun. 12 (2021) 5554, https://doi.org/10.1038/s41467-021-25822-x.
[24] H. Hu, X. Lin, L.J. Wong, Q.R. Yang, D.J. Liu, B.L. Zhang, Y. Luo, Surface dyakonov–cherenkov radiation, eLight 2 (2022) 2, https://doi.org/10.1186/s43593-021-00009-5.

[25] M.P. Springstead, A.B. Zylstra, Y. Kim, K.D. Meaney, H. Geppert-Kleinrath, A. Leatherland, L. Wilson, H.W. Herrmann, C.S. Young, P. Polk, C. Hamilton, Solid Cherenkov detector for studying nucleosynthesis in inertial confinement fusion, Rev. Sci. Instrum. 91 (2020) 073503, https://doi.org/10.1063/5.0002874.
[26] J. Jeet, A.B. Zylstra, V. Rekow, C.M. Hardy, N. Pelepchan, M. Eckart, Y. KimM. Rubery, A.S. Moore, D.J. Schlossberg, E. Folsom, The Vacuum Cherenkov Detector (VCD) for γ-ray measurements in inertial confinement fusion experiments, Rev. Sci. Instrum. 93 (2022) 103543, https://doi.org/10.1063/5.0101830.
[27] S. Moore, D.J. Schlossberg, E.P. Hartouni, D. Sayre, M.J. Eckart, R. Hatarik, F. Barbosa, J. Root, C. Waltz, B. Beeman, M.S. Rubery, G.P. Grim, A fused silica Cherenkov radiator for high precision time-of-flight measurement of DT γ and neutron spectra, Rev. Sci. Instrum. 89 (2018) 10I120, https://doi.org/10.1063/1.5039322.
[28] K.W. Jang, W.J. Yoo, S.H. Shin, J. Moon, K.T. Han, D. Jeon, Measurements of cerenkov lights using optical fibers, IEEE Trans. Nucl. Sci. 2 (60) (2013) 932–936.
[29] S.H. Law, S.C. Fleming, N. Suchowerska, D.R. McKenzie, Optical fiber design and the trapping of Cherenkov radiation, Appl. Opt. 36 (45) (2006) 9151–9159.
[30] Mei Zhang, Ji-Zhen Zhao, Yang Li, Liang Sheng, Quan Guo, Yan-Hong Zhang, Yuan Yuan, Yan Ma, Yi-Hong Yan, Investigation of radiation response on pure silica large core fibers at low dose levels, Nucl. Instrum. Methods Phys. Res. 1048 (2023) 167931, https://doi.org/10.1016/j.nima.2022.167931.
[31] I.M. Frank, I.E. Tamm, Coherent visible radiation of fast electrons passing through matter, in: Proceedings of the USSR Academy of Sciences, 1937, pp. 109–114.
[32] P. Coupé, P. Yger, S. Prima, P. Hellier, C. Kervrann, C. Barillot, An optimized blockwise nonlocal Means denoising filter for 3-D magnetic resonance images, IEEE Trans. Med. Imag. 4 (27) (2008) 425–441, https://doi.org/10.1109/TMI.2007.906087.
[33] V.G. Kleinrath, M.S. Freeman, C.R. Hurlbut, F. Merrill, J.R. Tinsley, P. Volegov, C. Wilde, A liquid VI scintillator cell for fast-gated neutron imaging, Rev. Sci. Instrum. 89 (2018) 101142, https://doi.org/10.1063/1.5039362.